(Received 29 August 2025, Accepted 26 November 2025, Scheduled 9 December 2025)

A Harmonic Suppression Algorithm for PMSMs Featuring Collaborative Dead-time and DC Bias Compensation

Yang Yu, Zehua Gong, and Xin Wang*

School of Electrical Information Engineering, Jiangsu University of Technology, Changzhou 213001, China

ABSTRACT: To enhance the stability of the spindle drive system in computer numerical control (CNC) machine tools and ensure machining accuracy by reducing non-ideal torque fluctuations caused by current harmonics during high-precision processes, a multi-factor harmonic current suppression algorithm based on an extended state observer (ESO) is proposed. Firstly, a mathematical model of the permanent magnet synchronous motor (PMSM) is established, and the current measurement offset errors (CMOEs) and their effects on the current waveform are analyzed in depth. Subsequently, zero-point lag phenomenon of the voltage source inverter (VSI) and its resulting harmonic characteristics are discussed in detail. Furthermore, the compensation principles for CMOE and VSI dead-time nonlinear distortion are elucidated, and a corresponding ESO structure is designed through theoretical derivation. The proposed method constructs a unified perturbation model and designs adaptive ESO to achieve cooperative compensation. A comparative analysis of the control strategy's performance before and after optimization validates the significant effectiveness of the proposed method in harmonic suppression. Experimental results show that the proposed strategy reduces the total harmonic distortion (THD) of the phase current to 3.28%, and key harmonics such as the 5th and 7th are suppressed to much lower levels. Torque ripple and speed fluctuation are significantly reduced, effectively improving the operational stability of the motor. The experimental results indicate that the proposed dual compensation scheme for dead-time and DC offset current can effectively reduce harmonic distortion and significantly enhance the operational performance of the PMSM.

1. INTRODUCTION

With the rapid advancement of modern computer numerical control (CNC) machine tools, permanent magnet synchronous motors (PMSMs) have been widely adopted in high-precision, high-efficiency applications. As core power sources in spindle drive systems, they stand out for their superior performance and high energy conversion efficiency. Nevertheless, current harmonics remain a critical issue. Primarily arising from phase current sensor measurement errors, these harmonics induce motor torque and speed ripples that degrade control performance [1–4]. This problem is further aggravated when the motor couples with low-resonance mechanical systems. In such cases, precision components like bearings, shafts, and gears may be damaged [5]. Consequently, suppressing PMSM current harmonics has become a key research focus. Beyond degrading control performance, current harmonics also accelerate the wear of precision components like motor bearings and shafting, shortening equipment service life and increasing maintenance costs; meanwhile, they lead to higher energy consumption, affecting the economy and continuity of CNC machining. Consequently, the suppression of PMSM current harmonics has become a key research focus.

Current harmonics mainly originate from two sources: current measurement offset errors (CMOEs) and dead-time effect. Dead-time introduces nonlinear distortion in the inverter output voltage. This produces high-frequency harmonic components, especially under light-load or low-speed conditions [6]. On the other hand, CMOEs manifest themselves as low-frequency drift and DC components. They disrupt d-q current decoupling, leading to static errors or oscillations [7]. To address these issues, researchers have proposed various suppression strategies.

For CMOE compensation, approaches include offline and online correction. Offline methods require costly, time-consuming calibration [8]. Moreover, due to closed-loop control, measured current errors may differ from actual errors [9]. Thus, most studies employ online estimation. In [10], the current measurement error is estimated via the d-axis current regulator output. However, this method requires complex rotor-position-dependent integration. In [11], phase-current calibration is achieved using DC-bus current sensing. This approach introduces additional hardware complexity. In [12], a method is proposed that demands specific speed/load conditions and involves algorithmic complexity. In [13], current measurement error (CME) is extracted via voltage error sequence components. Its accuracy is limited by the performance of the proportional-integral (PI) regulator. In [14], artificial errors are injected, and compensation is derived from speed harmonics. Nevertheless, this approach exacerbates pulsations during the injection process. In [15], vector reconstruction is utilized for harmonic separation. Yet the performance of this method depends on the harmonic suppressor. While these methods reduce the effects of DC offset, most of them neglect the impacts of dead-time.

* Corresponding author: Xin Wang (wx_simba@jsut.edu.cn).

For dead-time compensation, in [16], a neural-network band-pass filter is combined with an extended Kalman filter (EKF). Extracted harmonics are then used for voltage compensation. In [17] and [18], an adaptive linear neuron and a second-order generalized integrator are applied to extract the sixth-order harmonic, respectively. However, both approaches require extra controllers. In [19], dead-time is estimated from the q-axis current error. This method does not rely on accurate models but suffers performance degradation under complex conditions. In [20], a decoupled method is presented that exhibits good stability. Yet it is sensitive to parameter and delay errors.

In [21], a vector disturbance estimator is used to reduce fluctuations. Unfortunately, it amplifies noise simultaneously. In [22], a multi-composite coefficient filter is employed. This approach offers low cost, but its performance depends on rotor speed. In [23], currents are injected to compensate for voltage source inverter (VSI) nonlinearity. This results in strong low-speed performance, but precise tuning of the injection process is necessary. Nevertheless, these approaches generally overlook the influence of CMOE.

Currently, ESO and active disturbance rejection control (ADRC) are widely applied in harmonic suppression of PMSMs, but they exhibit significant performance limitations. Conventional linear ESOs have a fixed observation bandwidth, which prevents them from adapting to the dynamic variation characteristics of low-frequency disturbances. This results in insufficient estimation accuracy for such disturbances, making it difficult to meet the requirements of high-precision spindle drive systems for current harmonic suppression [27]. Two-stage ESOs require embedding a quasi-resonant controller in their cascaded structure to match specific disturbance frequencies; their design relies on the known frequency characteristics of disturbances. When facing fluctuations in disturbance frequencies caused by speed variations during PMSM operation, their universality is greatly restricted [29].

The ESO-based dual-compensation strategy proposed in this paper has clear advantages in terms of principle. In terms of the disturbance observation mechanism, by designing a gain adjustment logic dynamically matched with the observation bandwidth, it breaks through the limitation of the fixed bandwidth of conventional linear ESOs. It can adaptively adjust the observation sensitivity according to the disturbance characteristics of CMOE and dead-time effects, thereby realizing the synchronous and accurate estimation of these two types of disturbances. In balancing noise suppression and response speed, an innovative observation structure combining error feedback and disturbance feedforward is adopted: high-frequency noise is adaptively attenuated through the feedback loop, while the fast response capability to disturbances is retained through the feedforward channel. Compared with the passive noise suppression method of fractional-order error ESOs that rely on fractional-order operators, the noise attenuation amplitude is significantly improved. Moreover, there is no need to introduce additional complex operators, which avoids the problem of parameter tuning coupling [30]. In terms of operating condition adaptability, by regarding both CMOE and dead-time effects as extended states of the system for unified observation, there is no need to rely on motor speed information to construct a compensation model. This fundamentally overcomes the limitation of the multi-complex coefficient filtering scheme in Reference [22], which requires adjusting filter coefficients according to the rotor speed. At the same time, it eliminates the error correction link that relies on PI regulators in traditional schemes, reduces the dependence on the modeling of motor parameters such as stator resistance and inductance, and mitigates the impact of parameter mismatch on compensation effects — making it more suitable for the variable-speed and variable-load operating conditions of CNC machine tool spindles.

2. MATHEMATICAL MODELING AND HARMONIC MECHANISM ANALYSIS

2.1. PMSM Mathematical Model

In the d-q (direct-quadrature) synchronous coordinate system, an ideal mathematical model of PMSM can be expressed as:

$$\begin{cases} u_d = R_s i_d + L_d \frac{di_d}{dt} - \omega_r L_q i_q \\ u_q = R_s i_q + L_q \frac{di_q}{dt} + \omega_r \left(L_d i_d + \lambda_f\right) \end{cases} \tag{1}$$

where u_d and u_q are the voltages of the d and q axes; i_d and i_q are the currents of the d and q axes; R_s is the stator resistance of the motor; L_d and L_q are the inductances of the d and q axes; λ_f is the flux of the permanent magnet; and ω_r is the angular velocity of the rotor. Equation (1) corresponds to the voltage equivalent circuit shown in Figure 1. It can be seen from Figure 1 that the mathematical model of the three-phase PMSM achieves complete decoupling.

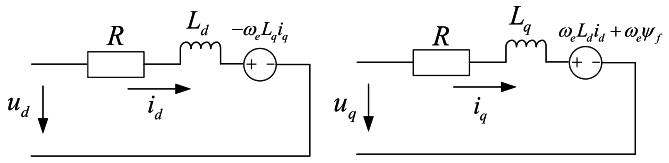

FIGURE 1. PMSM voltage equivalent circuit diagram.

The stator resistance limits the starting current, generates copper loss, and affects the starting stability and operating efficiency of the motor; the stator inductance stabilizes the speed and torque, suppresses current fluctuations and harmonics, and balances the starting current and response speed; the permanent magnet flux linkage provides the basis for electromagnetic torque generation, determines the maximum torque, and influences the back electromotive force and speed control strategy.

2.2. DC Bias Current

In PMSM, CMOE is caused by factors such as deviations of current measurement sensors, thermal drift of the sensors, and inaccuracies within the current feedback loop [24, 25]. These deviations directly affect the measured current values, which in turn generate current harmonics. Particularly in PMSM control systems, the DC offset current error leads to a series of adverse effects during motor operation, including the generation of harmonics, torque ripple, and a reduction in motor efficiency [26, 27].

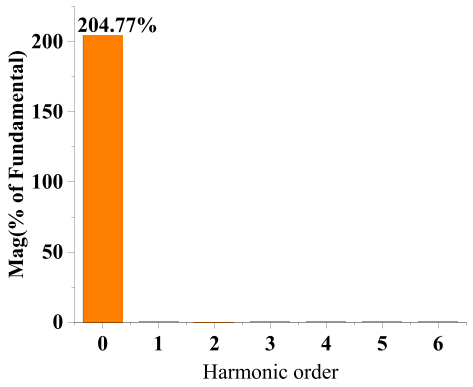

FIGURE 2. Harmonic analysis of q-axis current after DC bias addition.

When CMOE is present in the two-phase current sensors, the relationship between the measured current and actual current in the stationary reference frame can be expressed as:

$$\begin{cases} i_{a\_m} = i_a + i_{a\_oe} \\ i_{b\_m} = i_b + i_{b\_oe} \end{cases} \tag{2}$$

where i_{a_m} and i_{b_m} are the measured values; i_a and i_b are the actual values; i_{a_oe} and i_{b_oe} are the DC bias errors of the stator currents of phase a and phase b, respectively. Converting it to the d-q coordinate system gives:

$$\begin{cases} i_{d\_m} = i_d + i_{d\_oe} \\ i_{q\_m} = i_q + i_{q\_oe} \\ i_{d\_oe} = k_{oe} \sin\left(\omega_r t + \varphi\right) \\ i_{q\_oe} = k_{oe} \cos\left(\omega_r t + \varphi\right) \end{cases} \tag{3}$$

where ω_r is the rotor angular velocity; i_{d_m} and i_{q_m} are the measured value; i_d and i_q are the actual value; i_{d_oe} and i_{q_oe} are CMOEs of the stator current in the d and q axes; k_{oe} and φ are the amplitude and initial phase of the d-q axis CMOE, respectively, which can be expressed as:

$$\begin{cases} k_{oe} = \sqrt{i_{a\_oe}^2 + \frac{1}{3}\left(i_{a\_oe} + 2i_{b\_oe}\right)^2} \\ \varphi = \tan^{-1}\left[\sqrt{3} i_{a\_oe} / \left(i_{a\_oe} + 2i_{b\_oe}\right)\right] \end{cases} \tag{4}$$

According to Equation (3), the DC-form sampled bias current will generate a 1st harmonic current in the d-q current.

Through the fast Fourier transform (FFT) analysis of the phase current after adding the DC bias current error, it can be seen in Figure 2 that the DC bias primarily induces a significant DC component (harmonic order 0) in the q-axis current, with its magnitude reaching 204.77% relative to the fundamental component. In the d-q coordinate system, the DC bias current error is directly superimposed on the d-axis and q-axis components of the current signal, and appears as a sine or cosine signal with a fixed amplitude. The frequency of this signal is related to the speed of the motor, resulting in the generation of primary harmonics.

2.3. Dead-Time Effect

To avoid DC bus short circuits caused by switching delays (T_{on} and T_{off}) of the upper and lower power switches in the same bridge arm of the inverter, a dead-time (T_d) must be inserted into the PWM drive signals. This ensures the lower switch turns on only after the upper switch is fully turned off. In a PWM-controlled PMSM drive system, the dead-time effect is caused by the delay time generated during the switching process of the inverter's power switches [28]. When a time interval (the dead-time) exists between the turning off of one switch and turning on of its counterpart in the same phase leg, it leads to nonlinear distortion of the inverter's output voltage. This voltage distortion affects the current waveform of the PMSM, and the impact of the dead-time effect becomes more significant under low-speed or light-load conditions, generating prominent harmonic components [29].

To prevent a DC-link short-circuit, which could occur due to the unavoidable turn-on/turn-off time delays (T_{on} and T_{off}) of the IGBTs, a dead-time (T_d) is inserted into the gate drive PWM signals. During this dead-time period, the phase current flows through the freewheeling diodes, and the current path is dependent on the direction of the current. Therefore, considering T_d, T_{on}, and T_{off}, the significant dead-time-induced voltage error introduced in the phase 'a' output voltage is given by the following equation:

$$\Delta u_a = \frac{\left(T_d + T_{\text{on}} - T_{\text{off}}\right) U_{\text{dc}}}{T_s} \cdot \text{sign}(i_a) \tag{5}$$

where T_s and U_{dc} are sampling (switching) period and DC link voltage, respectively, $\text{sign}(i_a)$ can be expressed as

$$\text{sign}(i_a) = \begin{cases} 1, & i_a > 0 \\ -1, & i_a < 0 \end{cases} \tag{6}$$

In the d-q axis synchronous coordinate system, the voltage error caused by dead-time can be expressed as a Fourier series expansion:

$$\begin{cases} \Delta u_d = \frac{4kU_{\text{dc}}}{\pi T_s} \sum_{n=1}^{\infty} \frac{12n}{36n^2-1} \\ \Delta u_q = \frac{4kU_{\text{dc}}}{\pi T_s} \left\{-1 + \sum_{n=1}^{\infty} \frac{2\cos(6n\omega_e t)}{36n^2-1}\right\} \end{cases} \tag{7}$$

where Δu_d and Δu_q are the d-axis and q-axis voltage harmonics caused by dead-time effects in the inverter; k is the dead-time coefficient (related to dead-time duration and switching characteristics), where $k = T_d + T_{\text{on}} - T_{\text{off}}$; T_s is the switching period; n is the harmonic order; ω_e is the electrical angular frequency of the motor; and t is the time.

Figure 3 shows the harmonic analysis of phase current after adding dead-time. The results indicate that the dead-time effect primarily introduces significant harmonics in the phase current, with the 5th harmonic reaching 4.37%, the 7th harmonic at 4.09%, the 11th harmonic at 1.92%, and the 13th harmonic at 1.97%. These harmonics are the result of the dead-time-induced sixth-order voltage harmonic in the d-q synchronous coordinate system, which maps to the 5th, 7th, 11th, and 13th harmonics in the phase current.

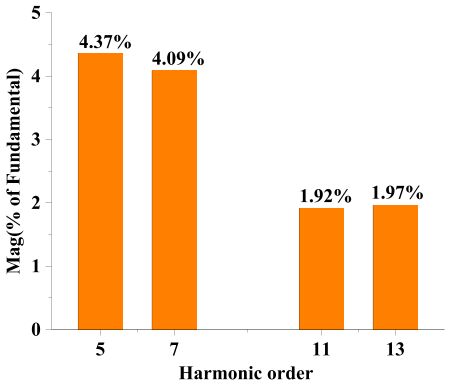

FIGURE 3. Harmonic analysis of phase current with dead-time included.

3. DEVELOPMENT OF HARMONIC SUPPRESSION STRATEGIES

In the previous section, this paper analyzes the effects of CMOE and dead-time on the signal, particularly the harmonic distortion problems they induce. To effectively mitigate these errors and optimize system performance, the following content will introduce the combined application of CMOE compensation and dead-time compensation. These two compensation methods are mutually complementary; by respectively compensating for the nonlinear distortions caused by DC offset and dead-time, they can work synergistically to significantly reduce errors and distortion in the signal, thereby enhancing the overall accuracy and stability of the system.

CMOE compensation addresses errors from circuit offsets, while dead-time compensation corrects nonlinear distortions caused by dead-time in the switching process. CMOE mainly causes low-frequency spectral distortion and disrupts the d-q axis current decoupling; the dead-time effect, on the other hand, leads to high-frequency harmonics and voltage errors. These two issues coexist and couple in practical systems, making it difficult to completely eliminate harmonics through single compensation alone. CMOE compensation stabilizes the low-frequency current components by offsetting the sensor offset error, while dead-time compensation improves the high-frequency voltage waveform by correcting the inverter nonlinearity. The two methods complement and cooperate with each other, enabling broadband harmonic suppression, and their overall performance is superior to that of a single compensation scheme. Next, this paper will discuss in detail the principles of these two methods and the advantages of their synergistic cooperation.

3.1. ESO for CMOE Estimation

For the mathematical modeling of PMSM, the voltage equation can be expressed as:

$$\begin{cases} u_\alpha = R_s i_\alpha + L_q \dot{i}_\alpha + e_\alpha \\ u_\beta = R_s i_\beta + L_q \dot{i}_\beta + e_\beta \end{cases} \tag{8}$$

where u_α and u_β are the α-axis and β-axis voltages of the PMSM stator windings; R_s is the stator resistance; i_α and i_β are the α-axis and β-axis currents of the stator windings; L_q is the quadrature-axis (q-axis) inductance; e_α and e_β are the sum of the PMSM equivalent back EMF shaft components. For convenience, in practice, the calculation of the equivalent back EMF observed by CMOE is simplified as:

$$\begin{cases} \hat{e}_\alpha = -\omega_r \psi_f \sin\theta_r \\ \hat{e}_\beta = \omega_r \psi_f \cos\theta_r \end{cases} \tag{9}$$

where $\hat{e}_\alpha$ and $\hat{e}_\alpha$ are the estimated values of the α-axis and β-axis back electromotive force (EMF) of the PMSM; ω_r is the electrical angular velocity of the motor; ψ_f is the amplitude of the permanent magnet flux linkage; θ_r is the electrical angle of the motor. The proposed scheme is derived from Equation (8), which is rearranged to:

$$\begin{cases} \dot{i}_{\alpha,\beta\_m} = \frac{u_\alpha - R_s i_{\alpha,\beta\_m} - e_\alpha}{L_q} + Z_{\alpha,\beta} \\ Z_{\alpha,\beta} = \frac{R_s}{L_q} i_{\alpha,\beta\_oe} + \dot{i}_{\alpha,\beta\_oe} \approx \frac{R_s}{L_q} i_{\alpha,\beta\_oe} \end{cases} \tag{10}$$

where $\dot{i}_{\alpha,\beta\_m}$ is the estimated derivative of the α-axis and β-axis current in the PMSM; $Z_{\alpha,\beta}$ is the disturbance term related to CMOE; i_{α,β_oe} is the α-axis and β-axis CMOEs in the PMSM. The core of ESO is to treat disturbances as extended states. When CMOE is considered a disturbance, ESO can be used to estimate the disturbance.

Due to CMOE, parameter mismatches (such as changes in R_s, L_s) and back electromotive force (back EMF) fluctuations will introduce nonlinear disturbances. We define these uncertainties as extended states. Let $d_{\alpha,\beta}$ represent the comprehensive disturbances of the α-β axes (including CMOE, parameter errors, and back EMF interference), according to (8), the extended state space model of the system can be rewritten as:

$$\begin{cases} \dot{i}_\alpha = -\frac{R_s}{L_s} i_\alpha + \frac{1}{L_s} u_\alpha - \frac{1}{L_s} e_\alpha + d_\alpha \\ \dot{i}_\beta = -\frac{R_s}{L_s} i_\beta + \frac{1}{L_s} u_\beta - \frac{1}{L_s} e_\beta + d_\beta \\ \dot{d}_\alpha = 0 \\ \dot{d}_\beta = 0 \\ y = \begin{bmatrix} i_\alpha \\ i_\beta \end{bmatrix} \end{cases} \tag{11}$$

where $i_{\alpha,\beta}$ are the original states of the system; $d_{\alpha,\beta}$ are the newly added extended states (characterizing unknown disturbances); y is the measurable current feedback signal.

To estimate both the original states $i_{\alpha,\beta}$ and the extended states $d_{\alpha,\beta}$ simultaneously, the ESO for the α-β axes is designed as follows:

$$\begin{cases} \dot{\hat{i}} = -\frac{R_s}{L_s} \hat{i} + \frac{1}{L_s} u - \frac{1}{L_s} \hat{e} + \hat{d} + \beta_1 (i - \hat{i}) \\ \dot{\hat{d}} = \beta_2 (i - \hat{i}) \end{cases} \tag{12}$$

where $\hat{i}$ and $\hat{d}$ are the observed values of $i_{\alpha,\beta}$ and $d_{\alpha,\beta}$ respectively; β_1, β_2 are the observer gains; $\hat{e}_{\alpha,\beta}$ is the estimated value

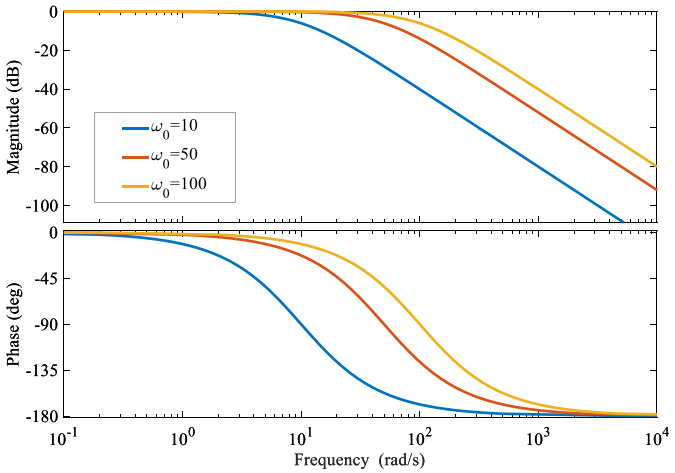

FIGURE 4. Bode plots analysis of ESO with different bandwidths.

of the back EMF. Therefore, for CMOE estimation, second-order ESO can be designed as:

$$\begin{cases} \varepsilon_{\alpha\beta} = i_{\alpha\beta\_m} - \hat{i}_{\alpha\beta\_m} \\ \dot{\hat{i}}_{\alpha\beta\_m} = \dfrac{u_{\alpha\beta} - \hat{R} i_{\alpha\beta\_m} - \hat{e}_{\alpha\beta}}{\hat{L}_q} + \hat{z}_{\alpha\beta} + \beta_1 \varepsilon_{\alpha\beta} \\ \dot{\hat{z}}_{\alpha\beta} = \beta_2 \varepsilon_{\alpha\beta} \end{cases} \tag{13}$$

where $\varepsilon_{\alpha\beta}$ is the estimation error of the α-β axis current; $\hat{i}_{\alpha\beta\_m}$ is the estimated α-β axis current; $\hat{R}$ is the estimated stator resistance; $\hat{L}_q$ is the estimated quadrature-axis (q-axis) inductance; $\dot{\hat{z}}_{\alpha\beta}$ is the estimated disturbance term (related to CMOE and other nonlinear factors); β_1 and β_2 are the gain of ESO. These parameters can be designed as: $\beta_1 = 2\omega_0$, $\beta_2 = \omega_0^2$, where ω_0 is the bandwidth of ESO.

The mismatches of motor parameters and the calculation errors of the utilized signals are taken into account, that is:

$$\begin{cases} \hat{R}_s = R_s + \Delta R_s \\ \hat{L}_q = L_q + \Delta L_q \\ \hat{e}_{\alpha,\beta} = e_{\alpha,\beta} + \Delta e_{\alpha,\beta} \\ \hat{u}_{s\alpha,\beta} = u_{s\alpha,\beta} + \Delta u_{s\alpha,\beta} \end{cases} \tag{14}$$

where ΔL_q is the deviation of q-axis inductance; $\Delta e_{\alpha,\beta}$ are the deviations of the equivalent back EMF; $\Delta e_{\alpha,\beta}$ may be caused by the variations of the parameters, such as ψ_f.

In (14), voltage errors, like $\Delta u_{sa,\beta}$ and $\Delta e_{\alpha,\beta}$, take the ac form, and their frequency is identical to the motor rotor speed in the stationary reference frame. The ac error components derived from $\Delta u_{sa,\beta}$ and $\Delta e_{\alpha,\beta}$ can be attenuated by the second-order Low-Pass Filter characteristics of the proposed ESO. Thus, the ESO with second-order LPF characteristics exhibits greater robustness against the calculation error of the equivalent back EMF induced by motor parameter variations and other factors.

As Figure 4 shows, frequency-domain analysis based on Bode plots is conducted. In the low-frequency range ($<$ 10 rad/s), all bandwidths maintain high gain (close to 0 dB), ensuring effective observation and compensation of low-frequency disturbances such as DC offset (0 Hz) and fundamental harmonics related to motor speed. For the medium-high frequency range (10 rad/s–1000 rad/s), a larger ω_0 results in slower amplitude decay, which enhances the observation gain for 6th-order harmonics (dominated by inverter dead-time) and 5th/7th-order mapped harmonics, thereby improving compensation accuracy. However, in the high-frequency range ($>$ 1000 rad/s), $\omega_0 = 100$ rad/s exhibits significantly higher gain than $\omega_0 = 50$ rad/s and $\omega_0 = 10$ rad/s, which easily amplifies high-frequency noise.

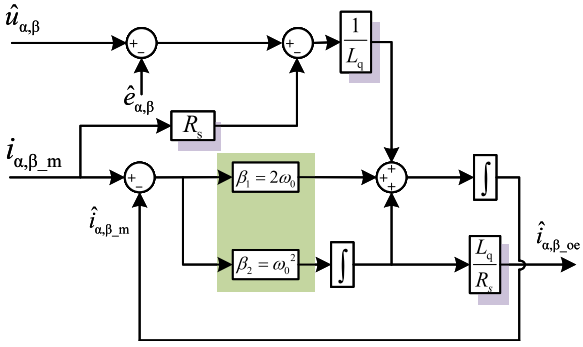

FIGURE 5. Block diagram of the CMOE estimation method based on ESO.

Considering that the ESO in this paper is specifically designed for estimating DC offset (a typical low-frequency disturbance with a frequency of 0 Hz), the bandwidth ω_0 is selected as 5 rad/s. This bandwidth value can not only ensure sufficient gain in the ultra-low frequency band to accurately capture and estimate the DC offset component, but also achieve rapid attenuation of high-frequency noise gain.

A block diagram of the proposed ESO-based CMOE estimation method is shown in Figure 5. In summary, this paper employs an ESO to estimate and compensate for the CMOE in a Permanent Magnet Synchronous Motor drive system. Compared to traditional methods, the ESO achieves accurate estimation of CMOE without relying on precise motor parameters by treating the CMOE as an extended state of the system. This leverages its powerful observation capabilities and reduces the requirements for system modeling accuracy. Simultaneously, the closed-loop observation structure of the ESO provides it with a fast dynamic response, enabling it to track changes in the CMOE in real time. This facilitates the dynamic compensation of CMOE, effectively suppresses low-frequency harmonics, and enhances both current control accuracy and system stability.

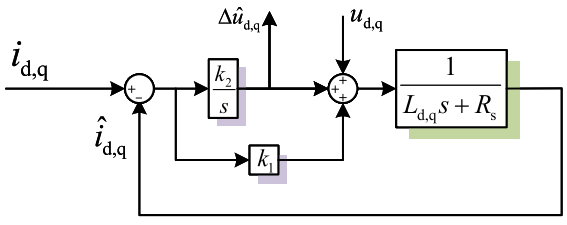

FIGURE 6. ESO dead-time compensation block diagram.

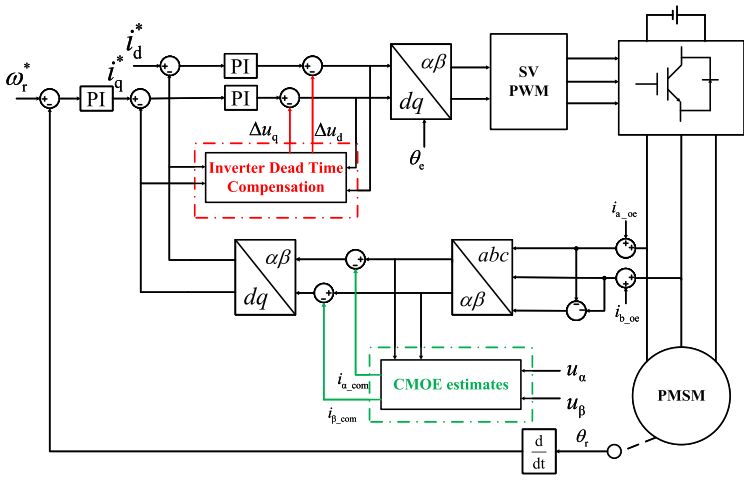

FIGURE 7. PMSM control block diagram with dead-time and DC bias current error compensation.

3.2. Dead-Time Compensation

Based on the dead-time compensation scheme for ESO shown in the Figure 6, ESO is used to estimate and compensate for voltage disturbances caused by dead-time. According to [30], the gain k_1 and k_2 designs of ESO are as follows: $k_1 = 2\omega_1$, $k_2 = \omega_1^2$, where ω_1 provides the bandwidth for ESO.

Compared to traditional dead-time compensation methods, the ESO does not rely on static or simplified models. In the face of complex dynamic changes and system nonlinearities, it can accurately compensate for current waveform distortion, overshoot, or system response lag caused by the dead-time effect, while tracking and correcting errors in real time. In the case of parameter mismatch, the ESO can reduce system errors and enhance control accuracy through real-time state estimation and compensation, thereby avoiding the dynamic instability or large errors that result from such mismatches. Compared to conventional methods, the ESO is able to maintain system stability and tracking accuracy to a greater extent.

3.3. System Block Diagram

Figure 7 shows the block diagram of the PMSM control system employing both DC offset current error compensation and dead-time compensation. In this scheme, these two methods are combined to optimize the control performance of the PMSM. The CMOE compensation scheme reduces the DC component in the current waveform and improves current accuracy and system stability by precisely estimating and compensating for CMOE caused by factors like sensor drift and system nonlinearities. Concurrently, the dead-time compensation scheme dynamically estimates and compensates for the dead-time effect using an ESO, effectively suppressing the nonlinear impact of switching actions and thereby significantly reducing the control error introduced by dead-time. The combination of these two allows the control system to not only accurately compensate for errors from DC offset current but also effectively mitigate the adverse effects of dead-time.

Through the synergistic action of these two schemes, the control accuracy and dynamic response performance of the PMSM are significantly improved. The system maintains high robustness, especially when facing parameter mismatches or external disturbances. This combined application enables comprehensive suppression of harmonic currents in the system, eliminating harmonic components that cannot be effectively compensated for by traditional control methods, thus significantly enhancing overall system performance. The experimental results indicate that this combined strategy achieves efficient and stable current control under various operating conditions, greatly improving the overall performance and reliability of the PMSM drive system.

4. EXPERIMENT

Table 1 presents the parameters of the PMSM used in the experiment.

TABLE 1. Parameters of the PMSM.

Parameters	Value	Parameters	Value
Rated power (P_r)	0.2 kW	Rated current (I_s)	2.1 A
Stator resistance (R_s)	1.6 Ω	Permanent magnet flux linkage (ψ_f)	0.0 Wb
Inductance (L_s)	5.07 mH	Pole pairs	4
Rated voltage (U_{dc})	310 V	Rated torque (T_e)	0.64 N·m

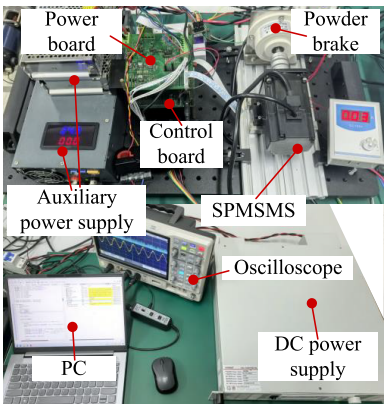

FIGURE 8. PMSM experimental platform.

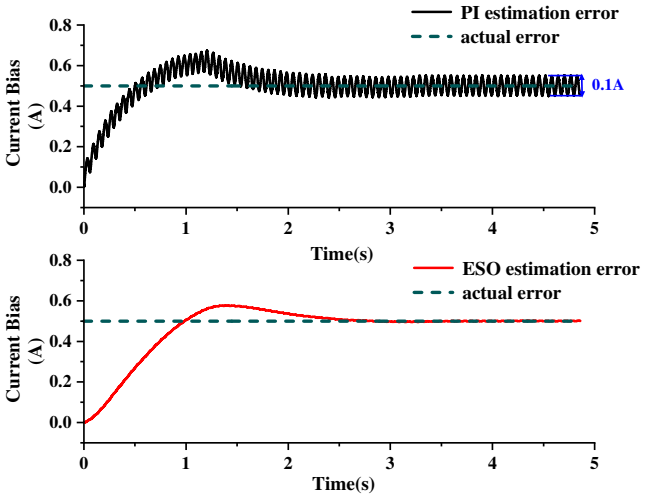

FIGURE 9. Comparison of the effectiveness of two bias current estimation schemes.

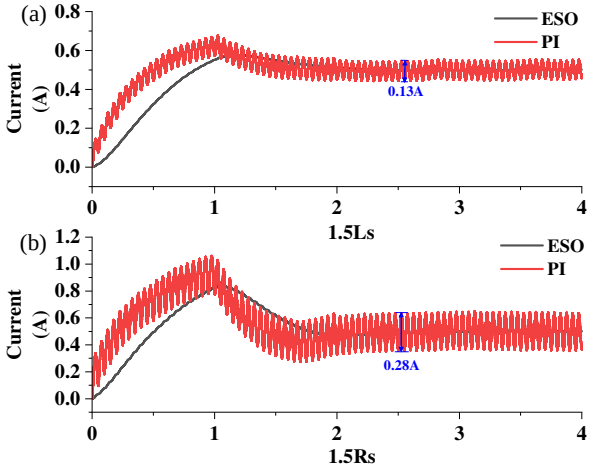

FIGURE 10. Effect diagram of CMOE estimation under parameter mismatch.

Figure 8 shows the composition of the experimental platform employed in the experiment. The control core adopts the TMS320F28335 DSP, the power driver board uses the Mitsubishi PS21965, and the software environment is configured as CCS 12.0.

The experiment adopts space vector pulse width modulation (SVPWM) as the PWM strategy, with a sampling frequency, PWM switching frequency, and current loop update rate all set to 10 kHz, and a speed loop update rate of 1 kHz.

Since the dead-time effect is most pronounced at low speeds, the motor speed is set to 300 r/min in the experiments. This setting maximizes the influence of the dead-time effect, thereby verifying the effectiveness and superiority of the proposed scheme.

During the FFT analysis, the fundamental frequency is set to 20 Hz, and one cycle is selected each time.

For the two bias current estimation schemes, namely the PI and the proposed ESO, in Figure 9, the PI estimation scheme has a settling time of approximately 1–1.5 seconds, with a steady-state error fluctuating between 0.45 A and 0.55 A, and its root mean square (RMS) estimation error can be approximated as 0.035 A due to sinusoidal-like fluctuations. In contrast, the proposed ESO estimation scheme in this paper has a settling time of less than 1 second, a steady-state error close to 0.5 A with negligible deviation, and an extremely small RMS estimation error (near zero). Based on the above quantitative metrics, it can be concluded that the ESO outperforms the PI significantly in terms of convergence speed, steady-state accuracy, and estimation stability for CMEO estimation.

Figure 10 presents a comparison of the estimation effects of the proposed ESO and the traditional PI method on CMOE under parameter mismatch scenarios. The robustness and estimation accuracy advantages of the ESO method are verified through two typical parameter mismatch conditions.

When the stator inductance L_s is adjusted to 1.5 times of its actual value, the DC bias estimation error of the PI method fluctuates drastically, with an average error range of approximately 0.13 A. Additionally, its convergence speed is slow, and there is no obvious trend of the error stabilizing throughout the observation process. When the stator resistance R_s is adjusted to 1.5 times of its actual value, the estimation performance of the PI method further deteriorates: the error fluctuation range expands to 0.28 A, and the deviation rate from the actual bias current exceeds 10%.

In contrast, regardless of whether there is inductance or resistance mismatch, the estimation error of the proposed ESO method is always controlled within the range of 0.48 A to 0.51 A, with an error fluctuation amplitude of only 0.03 A. This represents an 85.7% reduction in fluctuation amplitude compared to the PI method. Meanwhile, the ESO method quickly enters a stable estimation state after startup, with a convergence time shortened by more than 60% compared to the PI method, demonstrating stronger parameter robustness.

Figure 11 shows a comparison diagram of the phase 'a' current waveform of the motor before and after compensation. Without compensation, the current waveform has obvious distortion and serious harmonic interference. After compensation, the current waveform approaches an ideal sine wave, and the distortion is significantly reduced.

As shown in Figures 12, observing the motor's speed, a notable reduction in their fluctuations is evident after the compensation module is introduced at 2 seconds. This indicates improved stability in motor operation.

Analysis of Figure 13 shows that before compensation, the dq-axis current waveforms are severely distorted and oscillate at high frequencies, with a settling time exceeding 1.5 seconds; after compensation, they rapidly converge to a steady state within 0.5 seconds, and the steady-state error is nearly zero. From the perspective of machining precision, faster convergence enables the machining current to stabilize at the reference value more quickly, reducing machining errors caused by current fluctuations and thus improving machining precision and quality.

Figure 14 systematically demonstrates the remarkable superiority of the proposed method in harmonic compensation performance from two dimensions: the proportion of main har-

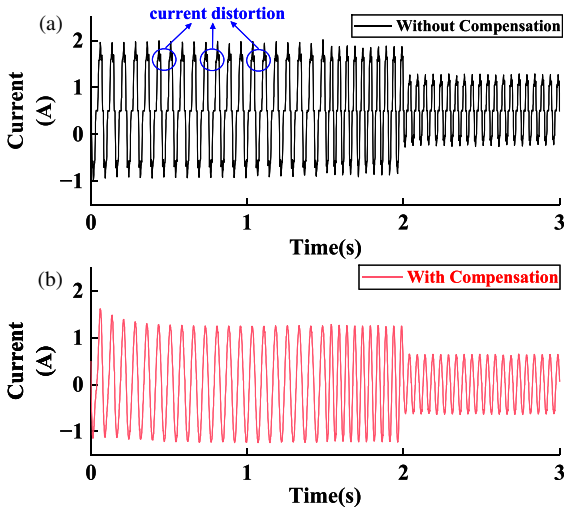

FIGURE 11. Compensation of phase current waveform before and after compensation.

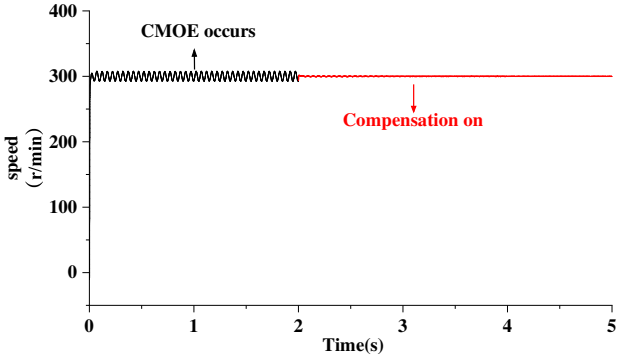

FIGURE 12. Diagram of speed before and after compensation.

monic orders of phase current (relative to the fundamental wave in percentage) and Total Harmonic Distortion (THD). In terms of harmonic suppression for each order, the EKF method has a fundamental wave harmonic proportion of 7.9%, and the proportions of the 5th, 7th, 11th, and 13th harmonics are 3.1%, 3.7%, 2.8%, and 2.1% respectively. Although the PI+ESO method reduces the fundamental wave harmonic proportion to 1.2%, the proportions of the 5th, 7th, and 13th harmonics instead climb to 4.7%, 4.5%, and 3.2%. In sharp contrast, the harmonic proportion of the proposed method in all analyzed harmonic orders is strictly constrained within the extremely low range of 0.2% to 0.4%, achieving uniform and strong suppression of each harmonic order.

When not compensated, the THD is as high as 54.5%, from the analysis of the total THD index, the THD of EKF is as high as 46.19%, that of PI+ESO is 8.76%, while that of the proposed method is only 3.28%, which is reduced by more than 92% compared with EKF and more than 62% compared with PI+ESO.

In summary, the proposed method demonstrates overwhelming advantages in both full-band precise harmonic suppression and extreme reduction of total distortion, which can control the phase current harmonic pollution at an extremely low level and

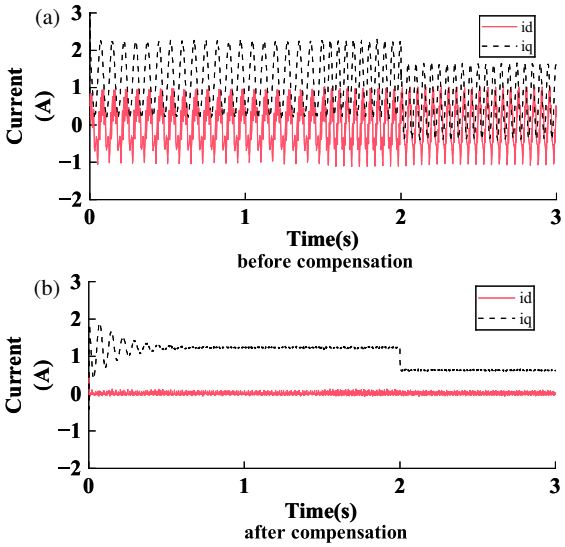

FIGURE 13. Comparison of d-q axis current before and after compensation.

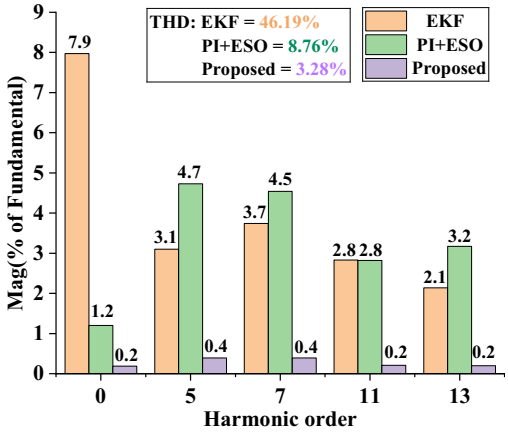

FIGURE 14. Comparison of harmonic suppression effects among different methods after compensation.

provide reliable current quality support for the efficient and stable operation of the motor system.

5. CONCLUSION

The comparative analysis reveals that the ESO-based DC offset compensation substantially outperforms the traditional PI method, delivering rapid convergence, smooth estimation, and high stability free from chattering or noise interference. Experimental results validate that the proposed dual-compensation strategy reduces the phase current THD from 46.19% (with EKF method) to 3.28% and significantly suppresses critical harmonics across main orders. Specifically, for the fundamental wave harmonic, it is reduced from 7.9% (EKF) and 1.2% (PI+ESO) to 0.2%; the 5th harmonic is cut from 3.1% (EKF) and 4.7% (PI+ESO) to 0.4%; the 7th harmonic is lowered from 3.7% (EKF) and 4.5% (PI+ESO) to 0.4%; the 11th harmonic is lowered from 2.8% to 0.2%; and the 13th harmonic is decreased from 2.1% (EKF) and 3.2% (PI+ESO) to 0.2%.

In detail, the ESO-based dead-time compensation accurately estimates and offsets inverter-induced voltage disturbances, while the ESO-based DC offset compensation effectively eliminates sensor-related offsets. Together, these two methods achieve synchronous and robust mitigation of two major nonlinear effects, enhancing current quality, reducing torque ripple, and improving spindle speed stability — all crucial for higher machining accuracy, better surface finish, and enhanced system reliability in CNC machine tools.

Notably, the experimental results from the 0.2 kW small-sized PMSM are fully applicable to CNC spindle accuracy improvement research. This is because small experimental motors and industrial CNC spindle PMSMs share the same core electromagnetic mechanism and mathematical model, with nonlinear harmonics from dead-time and CMOE being universal issues irrelevant to motor size or power. The proposed strategy relies on ESO's generalized disturbance estimation, independent of specific motor parameters — only minor ESO gain adjustments are needed for industrial spindles without changing the core logic.

Despite the promising outcomes, this study has limitations: it was validated under steady-state conditions, and performance under dynamic loads or extreme temperatures remains untested. Future research will focus on verifying the strategy under variable operating scenarios, optimizing ESO parameter adaptability for multi-power industrial motors, and reducing computational delay via hardware-software co-design to better support high-speed CNC spindle applications.

ACKNOWLEDGEMENT

This work was supported by the Natural Science Foundation of the Jiangsu Higher Education Institution of China (24KJB470011).

REFERENCES

[1] Lee, K.-W. and S.-I. Kim, "Dynamic performance improvement of a current offset error compensator in current vector-controlled SPMSM drives," *IEEE Transactions on Industrial Electronics*, Vol. 66, No. 9, 6727–6736, 2019.

[2] Bai, Y., B. Li, Q. Wang, D. Ding, G. Zhang, G. Wang, and D. Xu, "An adaptive-frequency harmonic suppression strategy based on vector reconstruction for current measurement error of PMSM drives," *IEEE Transactions on Power Electronics*, Vol. 38, No. 1, 34–40, 2023.

[3] Song, P., T. Wang, L. Wu, H. Li, X. Meng, and C. Li, "Analysis and compensation of current measurement errors in machine drive systems — A review," *Energies*, Vol. 18, No. 6, 1367, 2025.

[4] Dan, H., H. Pang, Y. Liu, Y. Sun, M. Su, M. Rivera, and P. Wheeler, "Current measurement errors compensation based on current ripple component decoupling for PMSM drives," *IEEE Journal of Emerging and Selected Topics in Power Electronics*, Vol. 13, No. 2, 1699–1709, 2025.

[5] Hu, M., W. Hua, Z. Wu, N. Dai, H. Xiao, and W. Wang, "Compensation of current measurement offset error for permanent magnet synchronous machines," *IEEE Transactions on Power Electronics*, Vol. 35, No. 10, 11 119–11 128, 2020.

[6] Zhang, N., Q. Song, M. Wang, and W. Zhang, "A dead-time compensation method for motor drive inverters based on nonlinear observer," *Computers and Electrical Engineering*, Vol. 120, 109668, 2024.

[7] Mandl, J., P. Trampitsch, P. Schachinger, D. Albert, R. Klambauer, and A. Bergmann, "Development of a fiber optic current sensor for low DC measurements in the power grid," *IEEE Transactions on Instrumentation and Measurement*, Vol. 73, 1–8, 2024.

[8] Zhao, J., W. Ou, N. Cai, Z. Wu, and H. Wang, "Measurement error analysis and compensation for optical encoders: A review," *IEEE Transactions on Instrumentation and Measurement*, Vol. 73, 1–30, 2024.

[9] Song, Z., X. Ma, and Y. Yu, "Design of zero-sequence current controller for open-end winding PMSMs considering current measurement errors," *IEEE Transactions on Power Electronics*, Vol. 35, No. 6, 6127–6139, 2020.

[10] Jung, H.-S., S.-H. Hwang, J.-M. Kim, C.-U. Kim, and C. Choi, "Diminution of current-measurement error for vector-controlled AC motor drives," *IEEE Transactions on Industry Applications*, Vol. 42, No. 5, 1249–1256, 2006.

[11] Lu, J., Y. Hu, G. Chen, Z. Wang, and J. Liu, "Mutual calibration of multiple current sensors with accuracy uncertainties in IPMSM drives for electric vehicles," *IEEE Transactions on Industrial Electronics*, Vol. 67, No. 1, 69–79, Jan. 2020.

[12] Kim, M.-S., D.-H. Park, and W.-J. Lee, "Compensation of current measurement errors due to sensor scale error and non-simultaneous sampling error for three-phase inverter applications," *Journal of Power Electronics*, Vol. 22, No. 1, 31–39, 2022.

[13] Kim, M., S.-K. Sul, and J. Lee, "Compensation of current measurement error for current-controlled PMSM drives," *IEEE Transactions on Industry Applications*, Vol. 50, No. 5, 3365–3373, 2014.

[14] Zhang, Q., H. Guo, Y. Liu, C. Guo, F. Zhang, Z. Zhang, and G. Li, "A novel error-injected solution for compensation of current measurement errors in PMSM drive," *IEEE Transactions on Industrial Electronics*, Vol. 70, No. 5, 4608–4619, 2023.

[15] Lee, S., H. Kim, and K. Lee, "Current measurement offset error compensation in vector-controlled SPMSM drive systems," *IEEE Journal of Emerging and Selected Topics in Power Electronics*, Vol. 10, No. 2, 2619–2628, 2022.

[16] Zhu, L., B. Xu, and H. Zhu, "Interior permanent magnet synchronous motor dead-time compensation combined with extended Kalman and neural network bandpass filter," *Progress In Electromagnetics Research M*, Vol. 98, 193–203, 2020.

[17] Qiu, T., X. Wen, and F. Zhao, "Adaptive-linear-neuron-based dead-time effects compensation scheme for PMSM drives," *IEEE Transactions on Power Electronics*, Vol. 31, No. 3, 2530–2538, Mar. 2016.

[18] Yan, Q., R. Zhao, X. Yuan, W. Ma, and J. He, "A DSOGI-FLL-based dead-time elimination PWM for three-phase power converters," *IEEE Transactions on Power Electronics*, Vol. 34, No. 3, 2805–2818, 2019.

[19] Han, K., X. Sun, B. Liu, W. Song, and X. Feng, "Dead-time on-line compensation scheme of SVPWM for permanent magnet synchronous motor drive system with vector control," *Proceedings of the CSEE*, Vol. 38, No. 2, 620–627, 2018.

[20] Lang, J., C. Tong, Y. Zheng, J. Bai, and P. Zheng, "Decoupled dead-time compensation method using revised-resonant control-based disturbance observer in PMSM drives," *IEEE Transactions on Power Electronics*, Vol. 40, No. 1, 340–350, Jan. 2025.

[21] Kim, S.-Y., W. Lee, M.-S. Rho, and S.-Y. Park, "Effective dead-time compensation using a simple vectorial disturbance estimator in PMSM drives," *IEEE Transactions on Industrial Electronics*, Vol. 57, No. 5, 1609–1614, May 2010.

[22] Wu, Z., H. Zhang, K. Liu, W. Hua, G. Zhang, B. Wang, S. Ding, and J. Hang, "Dead-time compensation based on a modified multiple complex coefficient filter for permanent magnet synchronous machine drives," *IEEE Transactions on Power Electronics*, Vol. 36, No. 11, 12 979–12 989, Nov. 2021.

[23] Yu, K. and Z. Wang, "An online compensation method of VSI nonlinearity for dual three-phase PMSM drives using current injection," *IEEE Transactions on Power Electronics*, Vol. 37, No. 4, 3769–3774, Apr. 2022.

[24] Zuo, Y., H. Wang, X. Ge, Y. Liu, S. Zhu, and C. H. T. Lee, "A simple current measurement scaling error compensation method for PMSM drives," *IEEE Transactions on Power Electronics*, Vol. 39, No. 11, 14 122–14 128, 2024.

[25] Song, P., Y. Wang, E. Ma, L. Wu, T. Wang, and H. Li, "Current measurement error compensation based on modified multiple complex-coefficient filters in PMSM drives," *IEEE Transactions on Power Electronics*, Vol. 40, No. 3, 4067–4079, Mar. 2025.

[26] Yu, X., X. Wu, T. Wu, D. Yang, Z. Lei, and S. Huang, "An FTSMO-based current measurement offset error compensation method in SPMSM drives," *IEEE Transactions on Industrial Electronics*, Vol. 72, No. 7, 6840–6851, Jul. 2025.

[27] Yang, J., W.-H. Chen, S. Li, L. Guo, and Y. Yan, "Disturbance/uncertainty estimation and attenuation techniques in PMSM drives — A survey," *IEEE Transactions on Industrial Electronics*, Vol. 64, No. 4, 3273–3285, Apr. 2017.

[28] Guo, H., T. Xiang, Y. Liu, Q. Zhang, Y. Wei, and F. Zhang, "Compensation method for current measurement errors in the synchronous reference frame of a small-sized surface vehicle propulsion motor," *Journal of Marine Science and Engineering*, Vol. 12, No. 1, 154, 2024.

[29] Zhang, X., Q. Xu, Y. Miao, X. Wu, Y. Wang, and L. Yi, "An improved generalized extended state observer for current harmonic compensation in dual three-phase PMSMs," *IEEE Transactions on Power Electronics*, Vol. 40, No. 5, 7136–7149, May 2025.

[30] Urasaki, N., T. Senjyu, K. Uezato, and T. Funabashi, "An adaptive dead-time compensation strategy for voltage source inverter fed motor drives," *IEEE Transactions on Power Electronics*, Vol. 20, No. 5, 1150–1160, 2005.